SAND2019-10135J

A Sensitive Mass Spectrometry Apparatus for Time-Resolved Studies of Gas-Phase Chemistry at High Pressures.

Leonid Sheps,* Ivan Antonov,§ and Kendrew Au

Combustion Research Facility, Sandia National Laboratories, Livermore, CA 94551, United States

ABSTRACT

We report the construction of a new experimental apparatus for direct time-resolved probing of high-pressure gas-phase chemical reactions by photoionization mass spectrometry. The apparatus uses a laser photolysis slow-flow reactor, capable of operating at P = 0.3 – 100 bar and T = 300 – 1000 K. We initiate reactions in homogeneous gas mixtures by the photolysis of appropriate radical precursor using laser pulses at repetition rates of 1 – 10 Hz. The reacting mixture is continuously sampled into a vacuum chamber, ionized by VUV photons from laboratory-based discharge lamps or from a synchrotron beamline, and analyzed by a custom-designed mass spectrometer. Soft near-threshold ionization by tunable synchrotron radiation enables spectroscopic quantification of many key intermediates and products of chemical reactions. A novel ionization scheme in the high-density region of the sample gas jet increases the experimental sensitivity 100-fold, compared with existing instruments, without compromising mass resolution. A 40-kHz pulsed reflectron time-of-flight mass spectrometer in the orthogonal acceleration geometry achieves simultaneous detection of all ionized species with 25-μs time resolution. We demonstrate the power of this apparatus by investigating the ethyl radical oxidation reaction using very dilute ($<10^{12}$ molecules·cm^{-3}) ethyl concentrations at pressures up to 25 bar.

* *To whom correspondence should be addressed*: lsheps@sandia.gov

§ Present address: Department of Physics and Astronomy, Northwestern University, Evanston, IL 60208

1. INTRODUCTION

Many problems at the forefront of gas-phase chemical physics involve systems of coupled temperature- and pressure-dependent chemical reactions. One example of such complexity is combustion chemistry, where numerous reactions (decomposition, association, isomerization, oxidation, insertion, abstraction, and metathesis) take place in parallel. These reactions may occur on complex potential energy surfaces (PES) with multiple radical or closed-shell intermediates.[1-2] Because chemically activated intermediates can be stabilized by molecular collisions, the mechanisms of such reactions may depend strongly on pressure. Direct probing of reactive species over wide pressure ranges is critical for full understanding of, e.g., combustion chemistry. However, experimental detection of key intermediates that are present in small concentrations is difficult, especially at pressures above 1 bar. To address this challenge, we continue to pursue powerful analytical methods for studies of complex gas-phase reactions in harsh environments, including at elevated temperatures and pressures.

The ideal probe method for chemical kinetics should be universally applicable, selective, sensitive, and multiplexed (able to detect many species at once). Gas-phase kinetics studies commonly employ mass spectrometry, optical absorption, and gas chromatography (GC). Of these, mass spectrometry (MS) fulfills the ideal requirements to the largest extent, because all atoms and molecules without exception can be ionized. MS involves sampling a small amount of gas out of the reactor, followed by ionization and detection of the ions as a function of mass to charge ratio, *m/z*. MS has high sensitivity and dynamic range, so that short-lived species may be detected alongside excess reactants and major products, present in much higher concentrations.

The application of MS to chemical kinetics has progressed for over seven decades in all aspects of the experiments, including reactors, mass analyzers, and ionization methods.[3] Early pyrolysis furnaces, used to measure the ionization energies (IE) of hydrocarbon radicals,[4-7] evolved into many diverse sources. Chemistry has been studied by MS in shock tubes,[8-9] fast-flow reactors (i.e. reaction times varied *via* the distance from inlet to sampling point),[10-11] photolysis reactors (reactions probed in real-time after initiation by short laser pulses),[12-14] flames,[15-17] and jet-stirred reactors.[18]

The performance of mass spectrometers has also continually improved. Initially, magnetic sector or quadrupole mass spectrometers detected one ion mass at a time. Later, fast-scanning sector MS[19] was developed for monitoring many ion peaks at once, but was soon eclipsed by the innovation of space focusing in time-of-flight mass spectrometry (TOF-MS) by Wiley and McLaren.[20] This technique is simple to construct and capable of rapid detection over very wide mass ranges.[21] The first use by Kistiakowsky of Wiley-McLaren TOF-MS, coupled to a flash photolysis reactor, achieved sampling rates of 20 kHz.[22] The introduction of reflectron TOF-MS enabled high mass resolving powers of $m/\Delta m > 3500$.[23] Lastly, orthogonal acceleration TOF-MS[24] has allowed pulsed TOF-MS apparatus to be used with continuous ionization sources, enabling efficient monitoring of evolving chemical systems in real time.

The choice of ionization source is just as important as the MS configuration to achieve time-resolved chemical analysis of complex reacting gas mixtures with isomeric selectivity. Early methods used 50 – 70 eV fixed-energy electron impact sources, which led to extensive fragmentation of the ions due to excess energy of ionization. (Typical IEs of organic molecules are in the 6 – 15 eV range). The characteristic ion cracking patterns are a good method of species identification, especially when coupled with separation

by GC. However, efficient real-time probing of reactions on sub-millisecond timescales leaves no time for chromatography, making time-resolved chemical analysis of complex mixtures very challenging by conventional electron impact ionization. Consequently, modern chemical kinetics studies favor "soft" electron ionization or photoionization at energies only slightly exceeding the IE of chemical species, thus avoiding ion fragmentation.

Numerous soft ionization approaches currently exist. Several groups use tunable low-energy electron impact ionization,[25] albeit typically with low intensity and energy resolution. Single- or multi-photon ionization by pulsed lasers or continuous atomic discharge lamps is also employed.[26-27] However, these schemes, too, have disadvantages. Laser methods have low repetition rates and are either not tunable (e.g. 9th harmonic of Nd:YAG), tunable but not intense (e.g. non-linear frequency up-conversion in rare gases), or not generally applicable (e.g. resonance-enhanced multi-photon ionization).[28] Discharge lamps do provide intense continuous radiation, but only at a few distinct energies. Most recently, synchrotron vacuum-ultraviolet photoionization mass spectrometry (VUV-PIMS)[29] became the most powerful ionization technique for chemical kinetics studies because it enables time-resolved spectroscopic species identification using soft ionization by continuous, bright, tunable VUV radiation.

The innovation in experimental methods continues today. Several state-of-the-art VUV-PIMS apparatus are now in use, employing photolysis reactors, molecular beams, jet-stirred reactors, aerosol sources, pyrolytic reactors, and flames.[30-31] A miniature shock tube with unprecedented repetition rates of up to 4 Hz was recently developed and coupled to synchrotron PIMS detection.[32] Sophisticated extensions of PIMS, e.g. synchrotron photoelectron-photoion coincidence (PEPICO) spectroscopy, are also becoming standard;[33] and recent improvement in the dynamics range of PEPICO detection[34] allows the application of PEPICO to chemical kinetics studies.[35]

The main benefit of synchrotron PIMS coupled to photolysis reactors is isomer-selective, multiplexed, time-resolved detection of chemical species, which is critical for constraining reaction mechanisms and validating chemical models. A schematic depiction of experimental data, obtained by VUV-PIMS with a photolysis reactor, is shown in Fig. 1. In these experiments, a low-repetition laser typically initiates reactions by photolysis of a radical precursor in a flowing gas mixture. Time-dependent mass spectra are recorded for every photolysis pulse and averaged over many pulses at each ionization energy E. The VUV photon energy is stepped over a range of E values, resulting in a 3D dataset of ion intensities $I(m/z, E, t)$ as a function of mass, ionization energy, and kinetic time t, relative to the photolysis pulse. Integration of the data over a range of t allows isomers of the same molecular mass to be distinguished by their photoionization (PI) spectra, while integration over specific ranges of E reveals isomer-selective product time traces.

Whereas synchrotron PIMS has been extensively applied in low pressure (1 – 50 torr) chemical kinetics experiments, its use in high-pressure studies is significantly more challenging because of two issues. One challenge is to achieve homogeneous environments at elevated temperatures (up to 1000 K) and pressures (up to 100s of bar). The reactor must ensure laminar flows with well-controlled spatial profiles and residence times. The orifice for sampling gas into the MS apparatus must be carefully designed to probe only gas-phase species and to minimize walls effects, e.g. the degradation of reactants or the destruction of intermediates and products. In photolysis reactors, the gas should be uniformly irradiated

by the photolysis laser. Diffusion at high pressures is slow, so that mass or heat transport timescales may approach those of chemical reactions (on the order of 0.001 s) and may interfere with the observed kinetics unless the sample is fully homogeneous from the start.

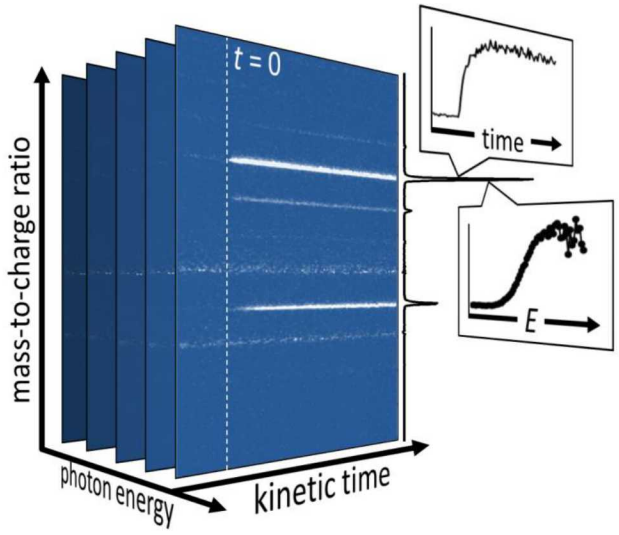

Figure 1. Schematic representation of the 3D dataset, generated by time-resolved VUV-PIMS, coupled to a photolysis flow reactor, in which reactions are initiated by a laser pulse at time $t = 0$ (dotted line).

The second challenge for high pressure PIMS is low sensitivity. Ideally, kinetics experiments over a range of total pressures vary the bath gas partial pressure but keep reactant partial pressures fixed, which increases the mixture dilution with increasing total P. Because the total sampling throughput is always limited by the pumping capacity of the MS vacuum chamber, increased dilution must be offset by higher detection sensitivity. This challenge is exacerbated for time-resolved studies, which must achieve the desired detection limits in each short time bin. For example, radical-radical reaction studies may require a detection limit of 10^{11} molec·cm^{-3} with sub-ms time resolution. This absolute number density is equal to a molar fraction of ~6 ppm at 1 Torr and 600K, which is easily achieved in existing PIMS apparatuses. However, the same detection limit at total P = 10 bar is equal to 0.8 ppb, which is below the sensitivity of existing instruments. Thus, realizing the full potential of VUV-PIMS for high-pressure kinetics studies requires an alternative mass spectrometer design.

In this paper we describe the construction of a new high-pressure chemical kinetics apparatus with time-resolved VUV-PIMS detection at Sandia National Laboratories. Although conceptually similar to earlier approaches of Fockenberg *et al.*,[27] Blitz *et al.*,[26] and Osborn *et al.*,[36] we made two major modifications. First, we initiate reactions by laser photolysis in a high-pressure (up to 100 bar), heated (up to 1000 K) flow tube, which achieves nearly ideal “0-D” reactor performance. Second, we probe these reactions by a new PIMS instrument, optimized for sampling from high-pressure sources (HP-PIMS). We use a novel high-density ionization scheme to increase ion yields 100-fold over conventional methods, as well as a custom mass spectrometer configuration to avoid ion-molecule collisions, resulting in high sensitivity and good mass resolution.

The HP-PIMS apparatus operates as a roll-up endstation at the Lawrence Berkeley Lab's Advanced Light Source (ALS) and takes advantage of the bright (10^{21} photons·cm^{-2}·sr^{-1}), narrowband ($E/\Delta E$ ~ 1000), tunable (7 – 25 eV) ionizing radiation from the Chemical Dynamics Beamline. Because beamtime at the ALS is limited, the HP-PIMS also uses continuous VUV radiation from a hollow-cathode discharge lamp in the laboratory at Sandia. Discharge-lamp operation produces useful kinetic data when monochromatic ionization is not required. Here we characterize the performance of HP-PIMS and discuss its application to hydrocarbon oxidation studies in low-temperature autoignition.

2. EXPERIMENT

2.1 High-Pressure Photolysis Reactor: Generating a homogeneous reaction environment without boundary-layer effects

We initiate the chemistry in our experiments by a photolysis laser in a slow-flow constant-*T*, constant-*P* high-pressure reactor (HPR), designed for a broad range of conditions (*P* = 0.3 – 100 bar, *T* = 300 – 1000 K). The HPR is a 4.770 in.-long, 3.000 in.-outer diameter (OD) Inconel chamber, consisting of the reactor body (4.300 in. long) and front flange (0.470 in. thick), as shown in Fig. 2. Premixed sample gas enters the reactor through one port at the back and exits through three ports at the front, equally spaced around the reactor circumference. Figure 2b depicts a cross-section cut through the reactor and highlights the details of its construction.

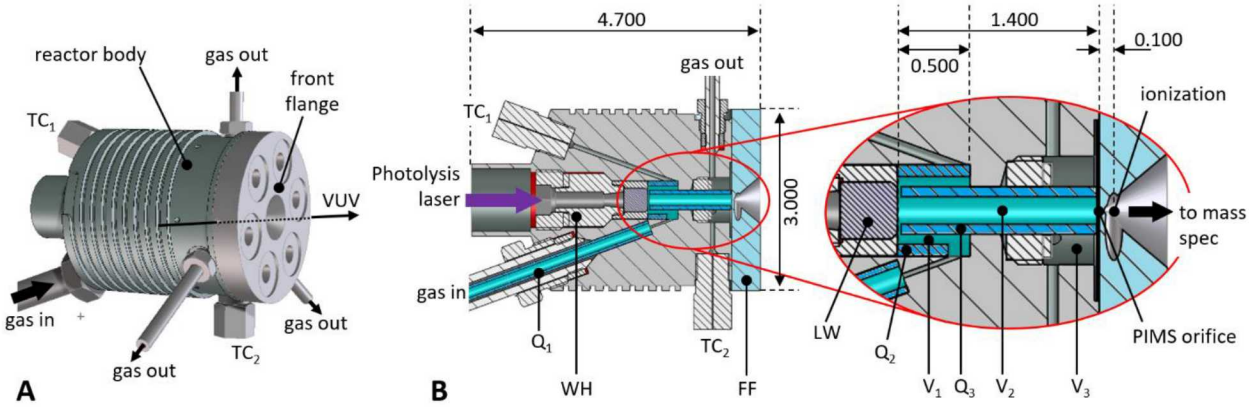

Figure 2. Overview (A) and cross-sectional (B) drawings of the high-pressure photolysis flow reactor used in the HP-PIMS apparatus. Inset on the right side shows an expanded view of the inner geometry of the reactor. Key features of the reactor are TC_1 – TC_2: thermocouple access ports; FF: front flange, WH: window holder, Q_1 – Q_3: quartz inserts; LW: laser window; V_1: pre-reaction volume; V_2: reaction volume; V_3: post-reaction volume. Dimensions are in inches. The VUV beam propagation is shown in panel A.

The inner volume of the reactor is bounded by the laser window at the back and the front flange at the front and is further separated into three regions (V_1 – V_3). The gas inlet is a 0.250-in. inner diameter (ID) bore, lined by a 0.16-in. ID tubular quartz insert (Q_1). After the inlet, the gas passes through an opening in a second tubular quartz insert (Q_2, OD = 0.630 in., ID = 0.472 in.) and flows to the left in Fig. 2 through the annular pre-reaction volume V_1. At the back of the reactor, the sample flows through a narrow (0.040 in.) gap between the laser window and a third quartz insert (Q_3, OD = 0.332 in., variable ID) towards the centerline of the vessel. Inside Q_3 the gas moves to the right through the reaction volume

V_2. The quartz inserts Q_1 – Q_3 protect the sample from most of the metal inner surfaces of the HPR and significantly reduce wall reactions. A small portion of the flow is sampled out of the HPR by an orifice in the front flange, while most of the gas exits V_2 *via* six channels (each with 0.5 mm^2 cross-section) in the front edge of Q_3, spaced equally around its circumference. The exhaust flows through the post-reaction volume V_3 and out of the reactor through three exit ports, located symmetrically around the HPR.

The HPR is heated by a resistive wire (Thermocoax, Inc.) with an Inconel sheath, wrapped tightly around the reactor and constrained in a helical groove (Fig. 2A). Two thermocouples (TC_1 and TC_2) provide temperature measurements in V_1 and V_3 (before and after the reaction zone), and a microprocessor controller maintains stable temperature by cycling AC current through the heating wire. A feedback-controlled needle valve (Research Control) regulates the pressure downstream from the outlet ports; two capacitance manometers monitor the inlet and outlet pressures. At normal operating conditions the TC_1 and TC_2 readings differ by no more that 1%, indicating a constant T profile along the reactor axis. The pressure drop from the inlet to outlet ports is less than 0.5% (i.e. is within the accuracy limits of the pressure gauges), which signifies constant sample *P*. Variable flows of bath gas, O_2, and trace reactants, premixed in the bath gas, are combined on-the-fly using calibrated high-pressure mass flow controllers (Bronkhorst); the sample passes through a helical static mixer before entering the HPR to ensure complete mixing of gasses.

The photolysis laser enters the HPR from the back through a 10 mm-thick UV Fused Silica window with a 4 mm-diameter open area and initiates reactions by photolysis of radical precursors. We use photolysis at 355, 266, or 213 nm, generated by the 3^{rd}, 4^{th}, or 5^{th} harmonic of an Nd:YAG laser (Continuum Surelite EX), or at 351, 248, or 193 nm from an excimer laser (Coherent Compex Pro). The sample mixtures are always optically thin, meaning that the laser fluence does not change along the axis of the HPR. We take care to maintain a spatially flat laser intensity profile, resulting in radially and axially homogeneous initial radical distributions. The reaction zone is 1.400 in. (~3.56 cm) long, and the internal volume V_2 is replenished (with additional safety margins of ~50%) between laser pulses. Typical experimental repetition rates are 1 - 10 Hz, which requires sample flow speeds of ~5 – 50 cm/s.

Part of the reacting gas is continuously sampled through an orifice into the PIMS apparatus as shown in Fig. 2B. It is ionized by a VUV beam, which propagates in a channel (ID = 0.120 in.), machined through the front flange perpendicular to the HPR centerline and 0.100 in. downstream of the sampling orifice, as shown in Fig. 2A. The HPR employs interchangeable orifices (0.005 – 0.05 mm dia.) and quartz inserts Q_3 (0.10 – 0.20 in. ID) for different experimental conditions. The orifices are laser drilled through 0.03-in. thick Ni disks, positioned before the front flange. We choose the orifice size to maximize gas throughput at a given pressure, not to exceed ~80 standard cubic centimeters per minute (SCCM), as limited by the pumping capacity of the HP-PIMS. The choice of Q_3 allows us to vary the reaction volume (V_2) from 0.18 to 0.72 cm^3. At higher *P* slow diffusion limits the influence of the wall and we use smaller ID inserts to reduce V_2 and the total sample flow. We seek compromise among experimental flexibility, sensitivity, and judicious use of gases by choosing appropriate Q_3 and orifice size to access a range of pressures (e.g. *P* = 1 – 10 bar, 10 – 20 bar, etc.) without having to re-configure the HPR.

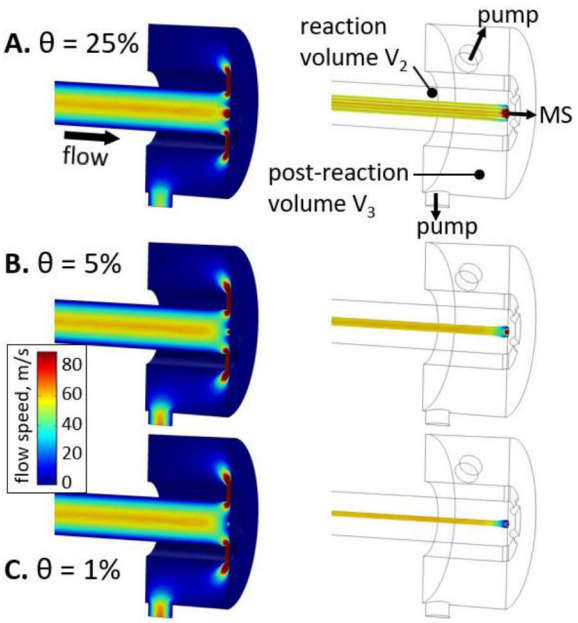

Figure 3. Simulated gas flow speed in the HPR at T = 600 K: *A*, P = 2 bar, total flow = 200 SCCM, θ = 0.25; *B*, P = 10 bar, total flow = 1000 SCCM, θ = 0.05; *C*: P = 50 bar, total flow = 5000 SCCM, θ = 0.01. The flow through the orifice is 50 SCCM in each case. The left side shows a cross-section of the entire gas charge, whereas the right side focuses only on the portion of the gas that is sampled into the HP-PIMS.

We optimized the HPR by fluid dynamics modeling using COMSOL Multiphysics software[37] to ensure that gas is sampled only from the center of the flow, while the wall boundary layer is diverted to the exhaust ports. The Navier-Stokes equations was solved for time-invariant laminar incompressible gas flow (Mach number M < 0.3) at 0.3 – 100 bar, 300 – 1000 K. The area within a few diameters of the sampling orifice cannot be modeled with incompressible flow equations, but this did not affect the simulations in the rest of the HPR. Additional tests using varying mesh dimensions and turbulent flows confirmed the validity of our results. The key parameter affecting the sample gas flow field is the fraction of the total gas flow that exits through the sampling orifice, which we define as θ. As reactor pressure increases, we use progressively smaller sampling orifices and consequently obtain a smaller value of θ. Figure 3 plots the simulated velocity profiles of the sample for three representative cases, θ = 0.25, 0.05, and 0.01, corresponding to typical operation at T = 600 K and total P = 2, 10, and 50 bar.

The results in Fig. 3 show that although the flow near the sampling orifice changes with experimental conditions, there are no recirculation zones and the sampled gas always comes from the center of the reactor. The flow field is radially symmetric up to the front end of V_2. The ballast volume V_3 separates the conductance limiting point, used for pressure regulation, from the reaction volume and helps to maintain the flow symmetry. The optimized design ensures that P, T, and linear speed in the HPR can be varied independently without compromising the sampling fidelity.

2.2 High-Pressure Mass Spectrometer: Improving sensitivity

The aim of our new high-pressure mass spectrometer is to increase the sensitivity of conventional PIMS detection without sacrificing other criteria necessary for chemical kinetics. In a typical PIMS apparatus the sampled gas expansion passes through a skimmer and forms a collimated molecular beam, which is

then ionized under collision-free conditions. The experimental signal is the ion count rate due to species i as a function of kinetic time t after photolysis, $S_i(t)$:

$$S_i(t) = Q_{tot} \cdot \chi_i(t) \cdot \sigma_i \cdot F_{VUV} \cdot \Lambda_{det} \quad \text{(E1)}$$

Q_{tot} is the total gas flow rate into the MS in units of molecules·s^{-1}, χ_i is the molar fraction of i (unitless), σ_i is the ionization cross-section (cm^2·photon^{-1}), and F_{VUV} is the total photon flux, integrated over the area of the ionizing beam (photons·s^{-1}). At the monochromator-equipped terminals of the ALS beamline 9.0.2, F_{VUV} can be adjusted from ~10^{11} to ~10^{13} photons·s^{-1} by choosing the width of the beam-defining apertures and the monochromator exit slits. Λ_{det} is an instrument-specific sensitivity factor:

$$\Lambda_{det} = O_{VUV} \cdot \tau_{VUV} \cdot \eta \quad \text{(E2)}$$

where τ_{VUV} is the time a molecule spends in the VUV beam (typically ~10^{-6} s), η is the mass-dependent ion collection efficiency (~0.1 – 1), and O_{VUV} is a VUV beam/gas jet spatial overlap factor – specifically, the fraction of sampled molecules that traverse the VUV beam per unit beam area (in units of cm^{-2}).

We chose to express Λ_{det} this way to make it independent of the VUV beam size, which may vary from one synchrotron or lab-based VUV source to another. Consider a small ionizing beam that intersect the center of a much larger gas jet in the horizontal plane, such that the jet density is relatively constant across the VUV beam area. If the VUV beam height is made larger, then the number of molecules traversing the beam increases proportionately to the beam area; neither O_{VUV} nor τ_{VUV} change. If the beam is made wider, then the same number of molecules traverse it; O_{VUV} decreases as the inverse of the beam area but τ_{VUV} increases linearly with the beam area. In any scenario, Λ_{det} does not depend on the beam size. Note that if the VUV beam were to approach the jet expansion in size, equations E1 and E2 could not be used. However, for HP-PIMS and other existing PIMS instruments E1 and E2 are valid.

Equations E1 – E2 can be used to estimate signals and compare the performance of different apparatus, operating at any location. In a typical PIMS apparatus that uses a 1-mm^2 VUV beam after a skimmer (e.g. 25 mm from the sampling jet), O_{VUV} ~0.1 cm^{-2} and Λ_{det} ~(1 – 10)×10^{-8} s·cm^{-2}, depending on η. In absolute terms, only ~0.1% of the sampled molecules are exposed to the ionizing photons.

Our goal is to decrease the minimum detectable quantity of analyte (χ_i) by maximizing the experimental sensitivity Λ_{det}. Equation E1 suggest two other approaches to increase sensitivity: increasing Q_{tot} or F_{VUV}. Increasing the former would require a proportional increase in pumping capacity, whereas the latter would require a higher flux light source. Both approaches are too costly and complex. Instead, we wish to enhance the detection efficiency by ionizing immediately after the sampling orifice, rather than after a skimmer. The density (ρ) in a free jet expansion drops as the square of the distance (x) from the orifice: $\rho \propto 1/x^2$. Therefore, ionizing closer to the orifice yields a dramatic improvement in the spatial overlap factor, O_{VUV}, and hence an increase in the number of ions produced.

Although our modification is conceptually simple, it leads to challenges that require a complete redesign of the mass spectrometer. The collection efficiency and mass resolution of TOF-MS depend on the ability to focus the ions into the acceptance volume inside the acceleration region of the mass analyzer, shown schematically in Fig. 4. Ion trajectories evolve in a six-dimensional position-velocity phase space (r_x, r_y, r_z, v_x, v_y, v_z) with mean ion expansion velocity $\langle\vec{v}\rangle$ directed along the *x*-axis. The transverse ion velocity

spread affects the acceptance volume and hence the detection efficiency: for ions to strike the detector, Δv_x, Δv_y must be small compared to the TOF extraction velocity along the *z*-axis. Even more critically, the spread of vertical positions Δr_z and velocities Δv_z must be small to minimize the spread of ion flight times (*ΔTOF*) and maximize mass resolution.

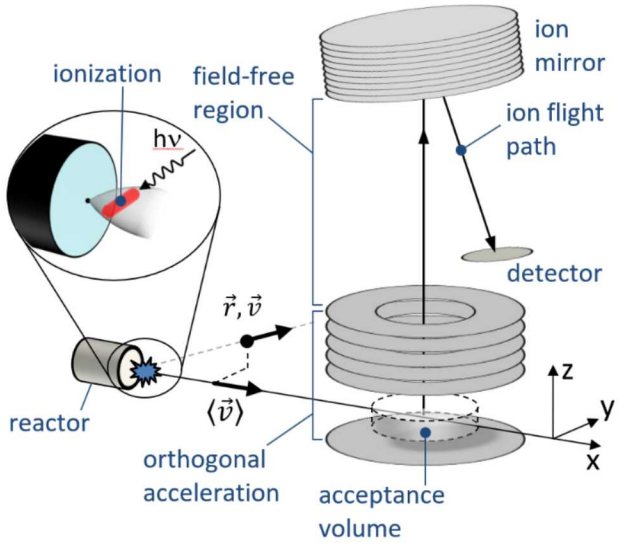

Figure 4. Schematic of an orthogonal acceleration reflectron TOF-MS. The sampling gas expansion propagates along the *x*-axis with mean velocity $\langle \vec{v} \rangle$. The inset shows the ionization volume for a horizontal VUV beam. The ion TOF direction is mainly along the *z*-axis. Any ion inside the spectrometer is characterized by its position vector $\vec{r}$ and velocity vector $\vec{v}$. The dotted lines define an acceptance volume for accelerated ions to strike the detector.

The challenge of our design is due to the location and size of the ionization volume. Ions that are born close to the orifice have a wide position and velocity distribution, i.e. occupy a large $\vec{r}$,$\vec{v}$ phase space, especially in the VUV beam direction. Moreover, focusing a wide-angle ion beam requires accelerating ions through a dense diverging neutral jet, leading to ion-neutral collisions, the possibility of ion-neutral reactions, and a further increase in the velocity distribution. Liouville's theorem states[38] that in the absence of dissipative forces the total ion phase space volume is conserved, so that electrostatic ion optics can reduce the spread in any $\vec{r}$ or $\vec{v}$ component only at the expense of the other components, provided that no ions are rejected.

We optimized the MS design using the SIMION 8.1 software package,[39] augmented with custom code to simulate ion-neutral collisions. We defined the neutral expansion properties *via* well-known analytic expressions[40] for the Mach number, density, and translational temperature. To simulate continuous gas sampling and ionization, we propagated a constant stream of ion trajectories, starting from a volume defined by the intersection of the VUV beam and the gas jet. The VUV beam at one of the 3-meter monochromator terminals at the ALS beamline 9.0.2 is dispersed vertically by a grating; it is typically 1 mm wide by 1 mm tall at the sample. We generated the initial ion spatial and velocity distribution by randomly sampling from the neutral jet position/velocity distribution within the ionization volume. An example simulation of the neutral expansion and initial ion packet is shown in figure 5 for the case of 0.02-mm dia. orifice and He bath gas at P = 10 bar, T = 600 K.

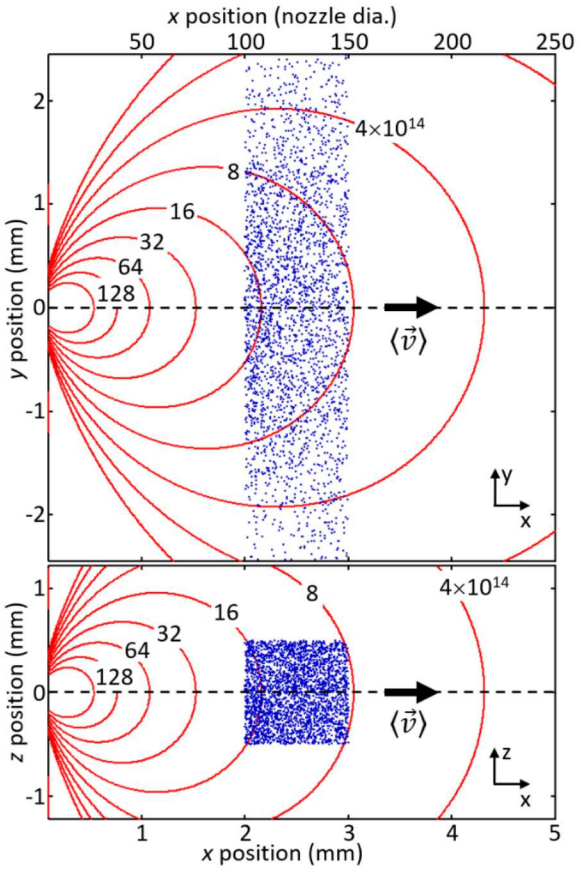

Figure 5. Simulated neutral jet density in the horizontal (top) and vertical (bottom) plane for a 0.02-mm dia. orifice and He bath gas, P = 10 bar, T = 600 K. Contour lines indicate gas density in units of 10^{14} cm^{-3}. Blue dots show the initial spatial distribution of 3000 ions, created by a 1×1mm VUV beam, propagating in the x-y plane. Mean ion beam velocity is indicated by $\langle\vec{v}\rangle$.

At each ion trajectory step, we treated interactions with the He bath gas as hard-sphere elastic collisions using a modified version of the HS1 collision model in SIMION 8.1.[39] We computed the probability and mean center-of-mass velocity of an encounter based on the molecular radii of the partners and the mean neutral density and velocity. The lab-frame orientation and impact parameter of each collision were chosen at random; the scattering angle and final ion kinetic energy were calculated. We neglected interactions with other ions and with all other neutral species due to their low concentrations. Key parameters in the MS design (physical arrangement and electrical potentials of ion optics, size and location of the VUV beam) were varied systematically. The predicted ion collection efficiency and mass resolution were evaluated for reactor pressures 0.3 – 100 bar and temperatures 300 – 1000 K. The optimal MS configuration results in simulated cumulative ion collision probability of ≤ 20%, best-case collection efficiency η ~0.5, and mass resolution m/Δm ~1600.

The optimized MS design is shown in Figures 6 – 7. Panel 6A is the overview of the vacuum chamber, which consists of 4 differentially pumped sections. The source region, evacuated by a 3200 L/s turbo pump (Osaka), houses the HPR and has optical access for the photolysis laser and the VUV ionization beam. The ion acceleration region contains most of the ion optics and is pumped by a 700 L/S turbo pump (Pfeiffer HiPace 700M). The pulsed ion acceleration stack is in a separate enclosure, pumped by a

third turbo pump (Pfeiffer HiPace 300M). Lastly, the ions travel vertically into a TOF tube, which holds a reflectron TOF mass analyzer and is pumped by a fourth turbo pump (Pfeiffer HiPace 700M). The base pressure throughout the chamber is ~$1 \cdot 10^{-8}$ Torr, whereas typical operating pressures are $P \leq 10^{-4}$ Torr in the source, $P \leq 10^{-5}$ Torr in the acceleration, and $P \leq 10^{-6}$ Torr in the TOF region.

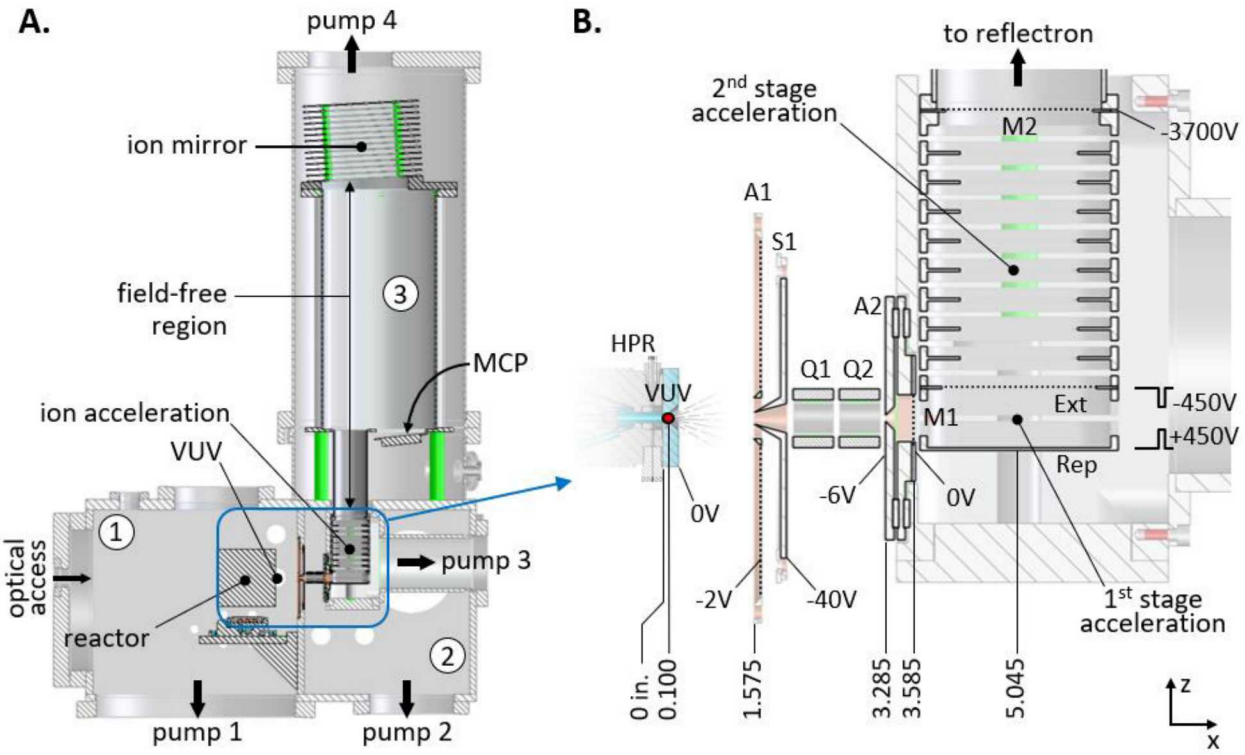

Figure 6. *Panel A*: overview of the experimental apparatus, consisting of 1) source, 2) ion acceleration, and 3) reflectron TOF region. The VUV ionizing beam propagates out of the figure plane. *Panel B*: detail view of the ion focusing and acceleration optics within the blue rectangle in panel A. HPR – reactor; A1 – aperture; S1 – skimmer; Q1, Q2 – quadrupole guides; A1 – aperture; M1 – mesh; Rep – repeller plate; Ext – extractor mesh; M2 – mesh. Key distances from the jet expansion along the *x* direction are listed in inches. The static (HPR, A1, S1, A2, M1, and M2) and pulsed potentials (Rep, Ext) are shown.

The key novel parts of the MS apparatus are detailed in Fig. 6B. The ionization volume is centered 0.100 in. (~2.5 mm) downstream of the sampling orifice, equal to 50 – 500 diameters for orifices 0.005 – 0.05 mm in dia. The ions propagate into the acceleration region through a slit skimmer S1, located 1.575 in. (~40 mm) from the orifice and nested within the aperture A1. The skimmer has a 1.58 in. wide by 0.16 in. high (~40×4 mm) opening, formed by a knife edge with included inner angle of 30°. A1 is a mesh disk with a 1.98 x 0.56 in. (~50×14 mm) opening. The HPR is electrically grounded, whereas A1 and S1 are held at -2V and -40V, respectively. This setup produces a 3-element cylindrical electrostatic lens that gently focuses the ion beam into the acceleration region. Figure 7 shows the equipotential contours of the ion focusing optics in the horizontal (xy) and vertical (xz) planes. Its key feature is that the electric field is initially flat and weak (so the ions move away from the dense region of the jet without strong acceleration that would induce collisions) but becomes stronger as the ions approach the skimmer.

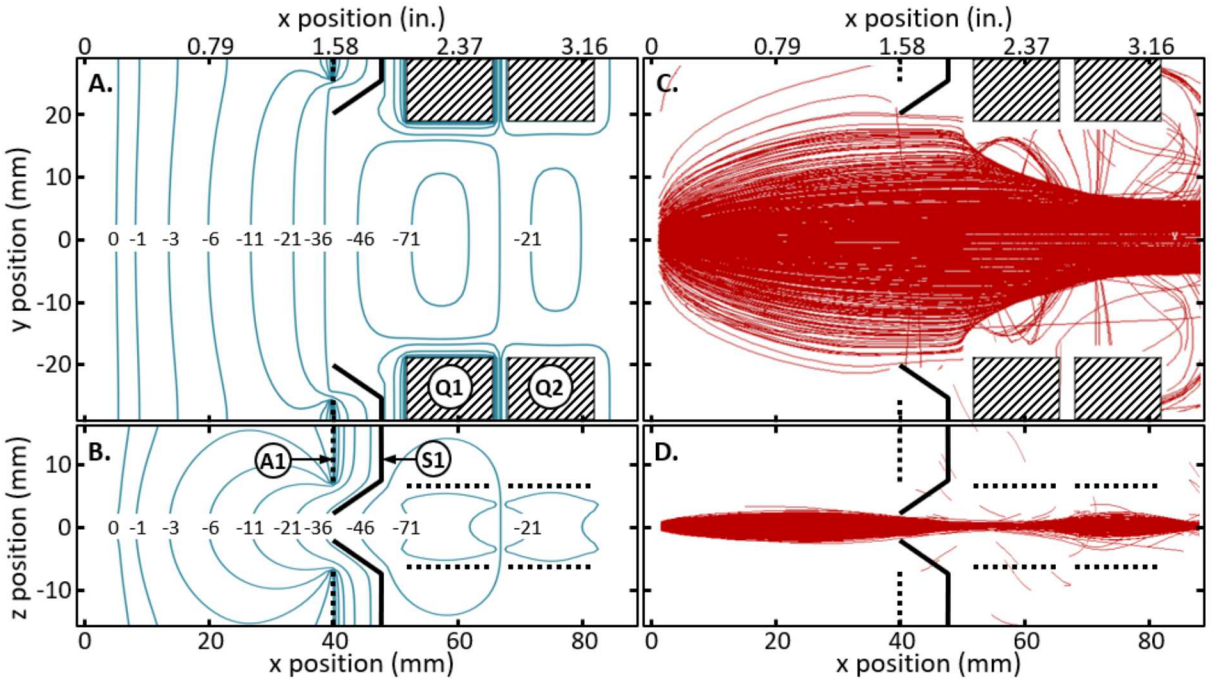

Figure 7. *Panels A, B*: simulated electric field contours (in V) in the horizontal (*A*) and vertical (*B*) planes. The location of A1, S1, Q1, and Q2 is marked. *Panels C, D*: 600 simulated trajectories for *m/z* = 58 ions.

Following the skimmer, the ions travel through quadrupole guides Q1 and Q2 that independently focus them in the vertical and horizontal planes, so that the wide initial r_y, v_y spread does not couple to the *z* dimension. Each guide is 0.55 in (14 mm) long and has cylindrical rods as the horizontal elements and mesh plates as the vertical elements. Next, the ions pass through a conductance-limiting aperture A2 and decelerating mesh M1 into the orthogonal acceleration zone. The first acceleration stage is made up of a repeller plate and extractor mesh, which are pulsed by a DEI PVM-4219 voltage switch to +350 V and -350 V, respectively at repetition rates up to 40 kHz. The second stage contains 8 plates with 40×40 mm square openings in the xy plane, and a mesh M2, connected by a resistor chain to provide a constant potential gradient down to -3700 V. During the 2 μs long, ± 350 V orthogonal extraction pulse, ions arriving from the source are electrostatically prevented from crossing mesh M1. After the previous ion batch leaves the acceleration stack, the repeller and extractor return to ground potential and ions from the source are again admitted through M1.

The ions proceed through a 22.6 in.-long field-free region, reflect at a 6° angle from a 2-stage ion mirror, and are focused onto an 80×30 mm rectangular microchannel plate (MCP) detector (Hamamatsu.) The 1st and 2nd stage of the ion mirror consists of 10 and 3 plates, respectively, with 5.00-in. round openings and a mesh located at the entrance of each stage. Rectangular meshes are crucial for good mass resolution in orthogonal TOF-MS;[41] therefore, our acceleration region and ion mirror have 95% transmitting Nickel meshes with 20×200 wires/in. density.

Ion counts from the capacitively-coupled MCP detector are conditioned by a preamplifier (Ortec) and a constant-fraction discriminator (LeCroy), recorded by a digitizer card (Fast Comtec MCS6A, 0.1 ns time resolution), and processed by a computer. A timing card (National Instruments) synchronizes the pulsed

TOF optics and photolysis laser. A Labview program parses the timestamp of each ion into its flight time (TOF) and kinetic time *t* after photolysis, so that time- and VUV energy-dependent mass spectra may be visualized in real time. When operating at the ALS, we monitor the VUV fluence using a calibrated SXUV-100 photodiode coupled to a picoammeter.

3. EXPERIMENTAL PERFORMANCE

We have operated the HP-PIMS apparatus and characterized its performance at temperatures of 300 – 800 K and pressures of 0.3 – 50 bar, using primarily He as the bath gas with variable partial pressures of O_2, 0 – 2 bar. Recently, we began to employ N_2 as the bath gas with good initial results; a description of the experimental performance with nitrogen as the major species will be forthcoming in future publications.

3.1 Mass Resolution

Mass resolution is measured daily using two calibration gas mixtures: A) 0.1% ethene/0.1% propene/ 0.1% 1-butene in balance Argon or B) 10% H_2/1% CH_4/0.5% Ar/0.1%Kr/0.1% Xe in balance Helium. The ion focusing depends mildly on the sample *T* but strongly on the *P* and on the sampling orifice diameter. Figure 8 shows a mass spectrum, obtained with ionization energy of 18 eV and flowing mixture B diluted in He at *P* = 2 bar and *T* = 600 K. The peaks are gaussian in shape, with widths m/Δm ~1800 (FWHM) across nearly the entire mass range. This performance provides sufficient resolving power to separate oxygenated compounds from hydrocarbons (e.g. C_4H_8O, *m/z* = 72.058, vs. C_5H_{12}, *m/z* = 72.094) up to 5 carbon atoms. With careful optimization, similar mass resolution can be obtained at all *T* and *P* that we surveyed.

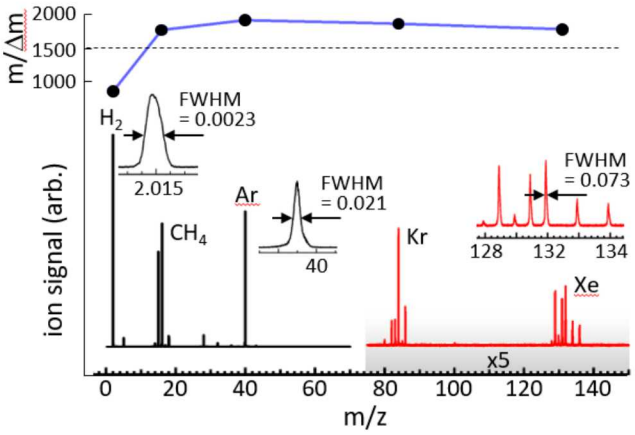

Figure 8. Mass spectrum, obtained by 18 eV ionization of calibration gas mixture B (10% H_2/1% CH_4/0.5% Ar/0.1% Kr/0.1% Xe), diluted in He at *P* = 2 bar and *T* = 600 K. The high mass region, *m/z* = 75 – 140, is magnified by a factor of 5 for clarity. The top graph shows the measured mass resolution, determined at *m/z* = 2 (H_2) 16 (CH_4), 40 (Ar), 83.9 (Kr), and 131.9 (Xe).

3.2 Sensitivity

We determined the sensitivity factor Λ_{det} using mass spectra of calibration mixture B, diluted in He and ionized at 18 eV. We measured the total sampling gas throughput into the HP-PIMS with calibrated flow meters and obtained the sampling rate of the analyte species from their molar fractions in the gas

mixture. We then computed Λ_{det} for CH_4, Ar, Kr, and Xe *via* Eq. E1, using the measured photon current and the published PI cross-sections of methane[42] and rare gases.[43] Figure 9 shows Λ_{det}, measured using a 0.01 mm.-diameter sampling orifice at T = 300 K and P = 1, 5, 10, 30, and 50 bar. The detection efficiency is mass-dependent, mainly because spatial focusing by the ion optics depends on the mass. The reason for this dependence is that ions produced in a supersonic expansion have the same initial beam velocity as the carrier gas, and hence different (mass-dependent) kinetic energies. Fig. 9 also shows that Λ_{det} depends on the sample pressure when using the same orifice, because higher P results in a greater number of ion-molecule collisions and increases the difficulty of ion focusing.

To quantify chemical species, detected by PIMS, it is essential that the experimental sensitivity is known precisely. Because Λ_{det} depends on the sample pressure and ion optics voltages, we measure it every time we change the orifice size or significantly alter the conditions in the reactor. We fit the measured Λ_{det} at m/z = 16, 40, 83.9, and 131.9 to smooth polynomial functions to interpolate it to other masses. In general, as Fig. 9 shows, we routinely achieve Λ_{det} ~$(1 - 10)\times10^{-6}$ s·cm^{-2} at P up to 50 bar, a roughly 100-fold increase in sensitivity, compared with other MS apparatus used for chemical kinetics studies.

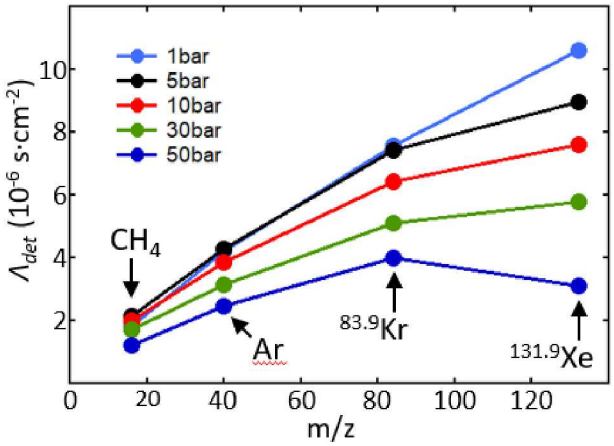

Figure 9. The sensitivity factor Λ_{det}, determined from the mass spectra of calibration mixture B (10% H_2/1% CH_4/0.5% Ar/0.1% Kr/0.1% Xe), diluted in He at T = 300 K and P = 1, 5, 10, 30, and 50 bar. The sampling orifice diameter was 0.01 mm, and ion optics settings were optimized at each pressure.

3.3 The oxidation chemistry of ethyl radicals

To demonstrate the power of the HP-PIMS apparatus, we probe the kinetics and product formation in the ethyl + O_2 reaction. This prototypical reaction has features common to the oxidation of many larger hydrocarbons.[44-45] It proceeds *via* two competing pathways: the formation of ethyl peroxy radicals that may later decompose, and a chemically activated (or formally direct) HO_2 production:

$$C_2H_5 + O_2 + M \rightleftarrows C_2H_5OO + M \qquad R_1; R_{-1}$$

$$C_2H_5 + O_2 (+M) \longrightarrow C_2H_4 + HO_2 (+M) \qquad R_2$$

Below $T \approx$ 500K R_1 dominates; the main product is stabilized ethyl peroxy, whereas the yield of HO_2 is low. At higher temperatures the decomposition of ethyl peroxy (R_{-1}) becomes important, resulting in appreciable concentrations of ethyl radicals in equilibrium with ethyl peroxy. This leads to rapid re-crossing *via* R_1 and R_{-1}, resulting in sharply increasing yield of HO_2 *via* reaction R_2. Although at high T and

P the direct HO_2 elimination from C_2H_5OO (R_3) is possible, it is not expected to be important at our conditions:

$$C_2H_5OO + M \rightarrow C_2H_4 + HO_2 + M \qquad R_3$$

Figure 10A shows the photoionization spectrum of the ethyl radical, C_2H_5, obtained in the HP-PIMS from two different precursors. We first generated 6.8×10^{11} cm^{-3} of ethyl radicals by direct photolysis of C_2H_5I at 248 nm in He at 400 K and 800 Torr. The concentration of C_2H_5 at t = 0 ms was computed from the starting $[C_2H_5I]$ and the measured photolytic depletion of its ion signal at m/z = 156. We also formed 1.4×10^{12} cm^{-3} of ethyl by Cl atom attack on ethane in excess He at 300 K and 800 Torr. Cl atoms were produced by 248-nm photolysis of Oxalyl Chloride, $(COCl)_2$, and initial $[C_2H_5]$ was obtained from the known concentration of ethane and its depletion using ion signal at m/z = 30. The PI spectra of C_2H_5 from both of these reaction schemes agree well with the published PI spectrum of ethyl.[46]

Figure 10B shows the time evolution of ethyl, measured by ionization at 9.3 eV, as a function of $[O_2]$ at 450 K and 1500 Torr. In these experiments C_2H_5 was produced by Cl-initiated H abstraction from ethane. Ethyl decay without O_2 is dominated by wall losses with a first-order rate coefficient $k_{decay} \approx 75$ s^{-1}. With increasing $[O_2]$ the decay becomes faster due to the reaction R_1 under pseudo-first order conditions. We fitted the ethyl signals to single-exponential decays and extracted a bimolecular rate coefficient from the slope of k_{decay} vs. $[O_2]$, as shown in the inset: $k_1 = (6.3 \pm 0.9)\times10^{-12}$ $cm^3\cdot molec^{-1}\cdot s^{-1}$.

We also measured the pressure-dependence of k_1 from 1 to 25 bar at T = 450 K, as plotted in Figure 10C. Our results compare favorably with the available experimental data at 580 Torr from Kaiser[47] and at 1.5 bar from Dilger *et al.*[48] Our results also agree well with the calculated values by Klippenstein and co-workers at 1 and 2 bar, although our measured pressure-dependence is somewhat steeper than the theoretical predictions.[49]

Notably, each measurement of the bimolecular rate coefficient (up to P = 25 bar) took only a few hours with low initial ethyl concentrations of $<1\times10^{12}$ cm^{-3}, which are required to avoid the complications from ethyl self-reaction. As an example, the data in Fig. 10B were taken with a 30 µm dia. orifice, so that the sampling throughput into the HP-PIMS was $Q_{tot} = 1.5\times10^{19}$ molecules$\cdot s^{-1}$. The initial ethyl concentration was 6.5×10^{11} cm^{-3} (molar fraction $\chi_i = 2\times10^{-8}$). The VUV flux was $F_{VUV} = 1\times10^{13}$ photons$\cdot s^{-1}$, as measured by the NIST-calibrated SXUV-100 photodiode, and the PI cross-section of ethyl at 9.3 eV is 3.9 Mb.[46] According to Fig. 9, the sensitivity for m/z = 29 ions is $\Lambda_{det} \approx 2\times10^{-6}$ $s\cdot cm^{-2}$, and from equation E1 we expect 23 ion counts$\cdot s^{-1}$ for the nascent ethyl radicals. The kinetic traces in Fig. 10B were averaged over 10,000 laser shots at a repetition rate of 10 Hz (~17 min. total acquisition time) and binned in 0.25 ms bins. Thus, we anticipate ~60 counts per time bin at time t = 0 ms, in good agreement with the observed values of ~50 counts/bin. Without the high sensitivity of HP-PIMS, each measurement would have taken about 100 times longer or would have produced much worse signal/noise ratios.

Figure 11A shows a time-resolved mass spectrum of the ethyl + O_2 reaction at 650 K and 1500 Torr, averaged over kinetic times t = 0 – 30 ms and VUV energies 9.8 – 11.2 eV. Approximately 4.5×10^{12} cm^{-3} ethyl radicals were produced by Cl-initiated H abstraction from ethane (as above) in He in the presence of 1×10^{18} cm^{-3} of O_2. At such high O_2 concentration, most ethyl radicals are promptly converted to ethyl peroxy, which does not have a stable parent cation and is instead observed via its fragment ion at m/z =

29.[50] On longer timescales the equilibrium distribution of ethyl and ethyl peroxy (which strongly favors C_2H_5OO at our conditions) decays to $C_2H_4 + HO_2$ *via* reaction R_2. The inset in Fig. 11A shows our measured spectrum of C_2H_4 at *m/z* = 28, compared to the reference spectrum of ethene.[51]

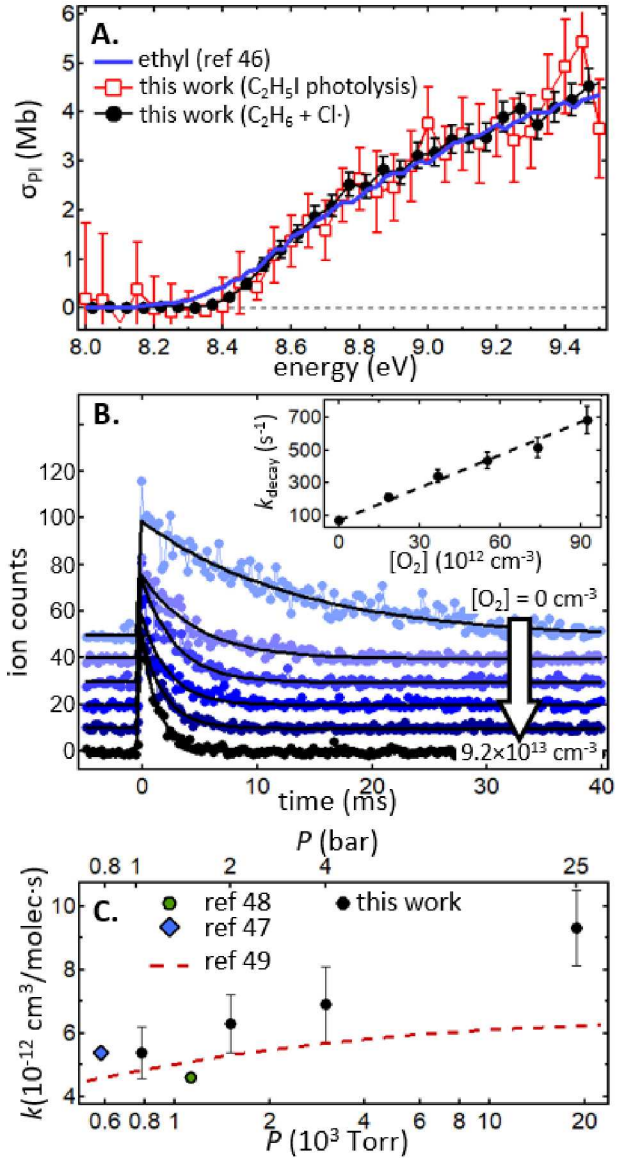

Figure 10. *Panel A*: The photoionization spectrum of ethyl radicals, produced either by direct 248-nm photolysis of C_2H_5I or by Cl atom attack on C_2H_6; the reference absolute PI spectrum of ethyl[46] is also shown. *Panel B*: The time evolution of ethyl radical ion signals at *m/z* = 29 as a function of O_2 concentration at T = 450 K and P = 1500 Torr. Inset shows the decay rate coefficient k_{decay} as a function of $[O_2]$. *Panel C*: The bimolecular rate coefficient for reaction $C_2H_5 + O_2 \rightarrow$ products as a function of pressure at T = 450 K, along with previously reported experimental and theoretical values.

Figures 11B and 11C present the kinetic traces of *m/z* = 28 and 29 ions (corresponding to ethene and C_2H_5OO, respectively) obtained at 11 eV at P = 1500 Torr and T = 550 – 650 K. We cannot quantify ethyl peroxy because its absolute PI cross-section has not been measured; however, we do quantify the C_2H_4

formation using the published absolute PI cross-section of ethene.[51] The traces in Fig. 11 show that C_2H_5OO are relatively stable at 550 K and that almost no C_2H_4 is produced. However, by 650 K ethyl peroxy radicals decay completely by 30 ms, forming ~4.2×10^{12} cm^{-3} of ethene on a similar timescale. Considering the 20% uncertainties on the PI cross-sections of ethyl and ethene, our measured yield of C_2H_4 corresponds to essentially complete conversion of ethyl to ethene, as we expect based on the published $C_2H_5 + O_2$ mechanisms.[44-45]

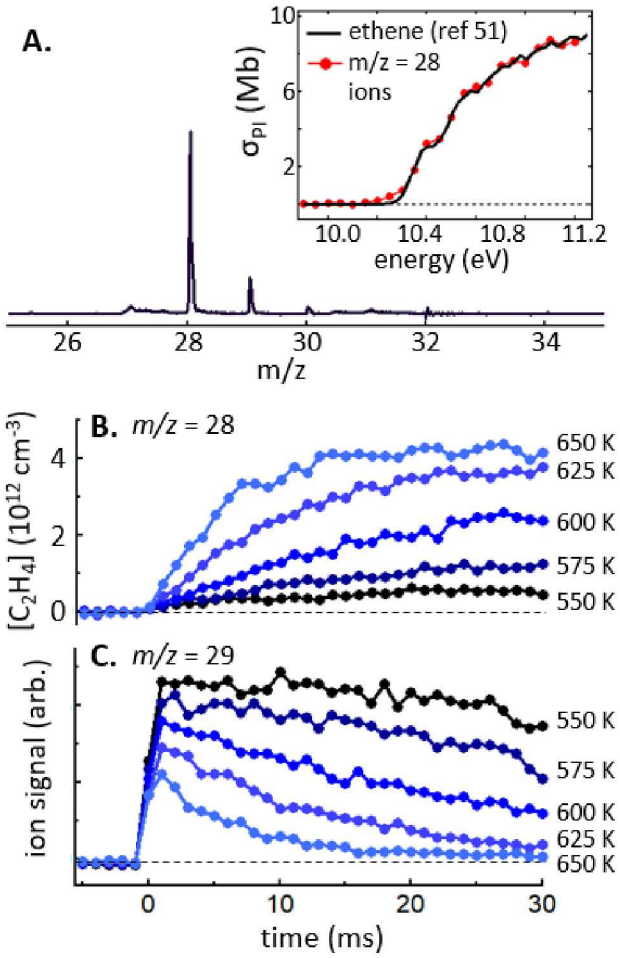

Figure 11. *Panel A*: Time-resolved mass spectrum (integrated over t = 0 – 30 ms and ionization energies 9.8 – 11.2 eV) of the ethyl + O_2 reaction at T = 650 K, P = 1500 Torr. Ethyl radicals were produced by Cl-initiated H abstraction from ethane using 248-nm photolysis of Oxalyl Chloride/C_2H_6/O_2 mixtures in excess He. The inset shows the PI spectrum of m/z = 28 ions, compared to a reference PI spectrum of ethene.[51] *Panel B*: Absolute concentration-time profiles of ethene, m/z = 28, at P = 1500 Torr and T = 550 – 650 K. *Panel C*: Time profiles of the ethyl peroxy ion counts (in arb. units), monitored *via* the fragment ion at m/z = 29 at T = 550 – 650 K. The initial ethyl concentration at t = 0 was ~4.5×10^{12} cm^{-3}.

4. CONCLUSION

We have constructed a new high-pressure PIMS apparatus for time-resolved experimental studies of gas-phase reactions at elevated temperatures and pressures. The apparatus employs a photolysis flow reactor, capable of operating at temperatures up to 1000 K and pressures up to 100 bar. Reacting gas is

sampled into a TOF mass spectrometer *via* molecular beam expansion and is ionized in a high-density region of the expansion, 2.5 mm downstream from the sampling orifice, using either fixed-wavelength output from discharge lamps or tunable monochromatic VUV synchrotron radiation.

The novel high-density ionization scheme, combined with a custom TOF design, results in significantly higher sensitivity (by a factor of ~100) than other recent PIMS apparatuses, allowing efficient detection of low-concentration chemical species. This increase in sensitivity is especially critical at high sample gas pressures of multiple bar, where the reactants molar fractions may need to be significantly lower, than at the more common experimental pressures of a few Torr. We demonstrated the potential of this apparatus by investigating the prototypical ethyl oxidation reaction at pressures up to 25 bar. Thanks to the sensitivity of HP-PIMS, we used C_2H_5 concentrations lower than ~1×10^{12} cm^{-3}, which allowed us to avoid the ethyl radical self-reaction and focus on the kinetics and products of the $C_2H_5 + O_2$ reaction. Our approach will enable similarly detailed studies of other radical reactions and the detection of low-yield products in complex reaction environments, e.g. in combustion and atmospheric chemistry.

5. ACKNOWLEDGEMENTS

This work was supported by the Division of Chemical Sciences, Geosciences and Biosciences, BES/USDOE, through the Argonne-Sandia Consortium on High Pressure Combustion Chemistry. Sandia National Laboratories is a multimission laboratory managed and operated by National Technology and Engineering Solutions of Sandia, LLC., a wholly owned subsidiary of Honeywell International, Inc., for the USDOE's National Nuclear Security Administration under contract DE-NA0003525. The Advanced Light Source is supported by the Director, Office of Science, Office of Basic Energy Sciences, of the U.S. Department of Energy under Contract No. DE-AC02-05CH11231. The views expressed in the article do not necessarily represent the views of the U.S. Department of Energy or the United States Government.

References

1. Osborn, D. L., Reaction Mechanisms on Multiwell Potential Energy Surfaces in Combustion (and Atmospheric) Chemistry. *Annu. Rev. Phys. Chem.* **2017**, *68*, 233-260.
2. Guo, H., Quantum Dynamics of Complex-Forming Bimolecular Reactions. *Int. Rev. Phys. Chem.* **2012**, *31*, 1-68.
3. Carr, R. W., Flash Photolysis with Time-Resolved Mass Spectrometry. *Adv. Photochem.* **1999**, 1-58.
4. Eltenton, G. C., The Study of Reaction Intermediates by Means of a Mass Spectrometer Part I. Apparatus and Method. *J. Chem. Phys.* **1947**, *15*, 455-481.
5. Hipple, J. A.; Stevenson, D., Ionization and Dissociation by Electron Impact: The Methyl and Ethyl Radicals. *Phys. Rev.* **1943**, *63*, 121.
6. Lossing, F.; Tickner, A., Free Radicals by Mass Spectrometry. I. The Measurement of Methyl Radical Concentrations. *J. Chem. Phys.* **1952**, *20*, 907-914.
7. Robertson, A. In *The Pyrolysis of Methane, Ethane and N-Butane on a Platinum Filament*, Proc. R. Soc. London, A, The Royal Society: 1949; pp 394-411.
8. Bradley, J.; Kistiakowsky, G., Shock Wave Studies by Mass Spectrometry. I. Thermal Decomposition of Nitrous Oxide. *J. Chem. Phys.* **1961**, *35*, 256-263.
9. Kern, R.; Singh, H.; Jhang, Q., Mass Spectrometric Methods for Chemical Kinetics in Shock Tubes. In *Handbook of Shock Waves*, 2001; Vol. 3, pp 77-105.
10. Atkinson, R.; Finlayson, B.; Pitts, J., Photoionization Mass Spectrometer Studies of Gas Phase Ozone-Olefin Reactions. *J. Am. Chem. Soc.* **1973**, *95*, 7592-7599.

11. Washida, N.; Bayes, K. D., The Reactions of Methyl Radicals with Atomic and Molecular Oxygen. *Int. J. Chem. Kinet.* **1976**, *8*, 777-794.
12. Ogryzlo, E.; Paltenghi, R.; Bayes, K. D., The Rate of Reaction of Methyl Radicals with Ozone. *Int. J. Chem. Kinet.* **1981**, *13*, 667-675.
13. Slagle, I. R.; Yamada, F.; Gutman, D., Kinetics of Free Radicals Produced by Infrared Multiphoton-Induced Decompositions. 1. Reactions of Allyl Radicals with Nitrogen Dioxide and Bromine. *J. Am. Chem. Soc.* **1981**, *103*, 149-153.
14. Slagle, I. R.; Gutman, D., Kinetics of Polyatomic Free Radicals Produced by Laser Photolysis. 5. Study of the Equilibrium Methyl + Oxygen ⇄ Ch_3o_2 between 421 and 538°. *J. Am. Chem. Soc.* **1985**, *107*, 5342-5347.
15. Foner, S.; Hudson, R., The Detection of Atoms and Free Radicals in Flames by Mass Spectrometric Techniques. *J. Chem. Phys.* **1953**, *21*, 1374-1382.
16. Cool, T. A.; McIlroy, A.; Qi, F.; Westmoreland, P. R.; Poisson, L.; Peterka, D. S.; Ahmed, M., Photoionization Mass Spectrometer for Studies of Flame Chemistry with a Synchrotron Light Source. *Rev. Sci. Instrum.* **2005**, *76*, 094102.
17. Hansen, N.; Cool, T. A.; Westmoreland, P. R.; Kohse-Höinghaus, K., Recent Contributions of Flame-Sampling Molecular-Beam Mass Spectrometry to a Fundamental Understanding of Combustion Chemistry. *Prog. Ener. Comb. Sci.* **2009**, *35*, 168-191.
18. Herbinet, O.; Battin-Leclerc, F., Progress in Understanding Low-Temperature Organic Compound Oxidation Using a Jet-Stirred Reactor. *Int. J. Chem. Kinet.* **2014**, *46*, 619-639.
19. Léger, E. G.; Ouellet, C., Kinetic Studies with a Fast-Scanning Mass Spectroscope. *J. Chem. Phys.* **1953**, *21*, 1310-1311.
20. Wiley, W. C.; McLaren, I. H., Time-of-Flight Mass Spectrometer with Improved Resolution. *Rev. Sci. Instrum.* **1955**, *26*, 1150-1157.
21. Mamyrin, B., Time-of-Flight Mass Spectrometry (Concepts, Achievements, and Prospects). *Int. J. Mass Spectrom.* **2001**, *206*, 251-266.
22. Kistiakowsky, G.; Kydd, P., A Mass Spectrometric Study of Flash Photochemical Reactions. I. *J. Am. Chem. Soc.* **1957**, *79*, 4825-4830.
23. Mamyrin, B.; Karataev, V.; Shmikk, D.; Zagulin, V., The Massreflectron, a New Non-Magnetic Time-of-Flight Mass Spectrometer with High Resolution. *Zh. Eksp. Teor. Fiz* **1973**, *64*, 82-89.
24. Guilhaus, M.; Selby, D.; Mlynski, V., Orthogonal Acceleration Time-of-Flight Mass Spectrometry. *Mass Spectrom. Rev.* **2000**, *19*, 65-107.
25. Casavecchia, P.; Leonori, F.; Balucani, N.; Petrucci, R.; Capozza, G.; Segoloni, E., Probing the Dynamics of Polyatomic Multichannel Elementary Reactions by Crossed Molecular Beam Experiments with Soft Electron-Ionization Mass Spectrometric Detection. *Phys. Chem. Chem. Phys.* **2009**, *11*, 46-65.
26. Blitz, M. A.; Goddard, A.; Ingham, T.; Pilling, M. J., Time-of-Flight Mass Spectrometry for Time-Resolved Measurements. *Rev. Sci. Instrum.* **2007**, *78*, 034103.
27. Fockenberg, C.; Bernstein, H. J.; Hall, G. E.; Muckerman, J. T.; Preses, J. M.; Sears, T. J.; Weston Jr, R. E., Repetitively Sampled Time-of-Flight Mass Spectrometry for Gas-Phase Kinetics Studies. *Rev. Sci. Instrum.* **1999**, *70*, 3259-3264.
28. Ng, C.-Y., Vacuum Ultraviolet Spectroscopy and Chemistry by Photoionization and Photoelectron Methods. *Annu. Rev. Phys. Chem.* **2002**, *53*, 101-140.
29. Taatjes, C. A.; Hansen, N.; Osborn, D. L.; Kohse-Höinghaus, K.; Cool, T. A.; Westmoreland, P. R., "Imaging" Combustion Chemistry *Via* Multiplexed Synchrotron-Photoionization Mass Spectrometry. *Phys. Chem. Chem. Phys.* **2008**, *10*, 20-34.
30. Qi, F., Combustion Chemistry Probed by Synchrotron Vuv Photoionization Mass Spectrometry. *Proc. Comb. Inst.* **2013**, *34*, 33-63.
31. Kostko, O.; Bandyopadhyay, B.; Ahmed, M., Vacuum Ultraviolet Photoionization of Complex Chemical Systems. *Annu. Rev. Phys. Chem.* **2016**, *67*, 19-40.
32. Lynch, P. T.; Troy, T. P.; Ahmed, M.; Tranter, R. S., Probing Combustion Chemistry in a Miniature Shock Tube with Synchrotron Vuv Photo Ionization Mass Spectrometry. *Anal. Chem.* **2015**, *87*, 2345-2352.
33. Tang, X.; Garcia, G. A.; Gil, J.-F.; Nahon, L., Vacuum Upgrade and Enhanced Performances of the Double Imaging Electron/Ion Coincidence End-Station at the Vacuum Ultraviolet Beamline Desirs. *Rev. Sci. Instrum.* **2015**, *86*, 123108.

34. Osborn, D. L.; Hayden, C. C.; Hemberger, P.; Bodi, A.; Voronova, K.; Sztáray, B., Breaking through the False Coincidence Barrier in Electron–Ion Coincidence Experiments. *J. Chem. Phys.* **2016**, *145*, 164202.
35. Sztáray, B.; Voronova, K.; Torma, K. G.; Covert, K. J.; Bodi, A.; Hemberger, P.; Gerber, T.; Osborn, D. L., Crf-Pepico: Double Velocity Map Imaging Photoelectron Photoion Coincidence Spectroscopy for Reaction Kinetics Studies. *J. Chem. Phys.* **2017**, *147*, 013944.
36. Osborn, D. L.; Zou, P.; Johnsen, H.; Hayden, C. C.; Taatjes, C. A.; Knyazev, V. D.; North, S. W.; Peterka, D. S.; Ahmed, M.; Leone, S. R., The Multiplexed Chemical Kinetic Photoionization Mass Spectrometer: A New Approach for Isomer Resolved Chemical Kinetics. *Rev. Sci. Instrum.* **2008**, *79*, 104103.
37. *Comsol Multiphysics*, Version 4.3; COMSOL, Inc.: Burlington, MA, USA.
38. Landau, L. D.; Lifshitz, E. M., *Mechanics*; Pergamon: Oxford, 1960.
39. Manura, D. J.; Dahl, D. A. *Simion 8.1*, Scientific Instrument Services, Inc.: Palmer, MA, USA.
40. Miller, D. R., Free Jet Sources. In *Atomic and Molecular Beam Methods*, University Press: Oxford, UK, 1988; Vol. 1, pp 14-53.
41. Selby, D. S.; Mlynski, V.; Guilhaus, M., Reducing Grid Dispersion of Ions in Orthogonal Acceleration Time-of-Flight Mass Spectrometry: Advantage of Grids with Rectangular Repeat Cells. *Int. J. Mass Spectrom.* **2001**, *206*, 201-210.
42. Samson, J. A. R.; Haddad, G. N.; Masuoka, T.; Pareek, P. N.; Kilcoyne, D. A. L., Ionization Yields, Total Absorption, and Dissociative Photoionization Cross Sections of Ch4 from 110 to 950 Å. *J. Chem. Phys.* **1989**, *90*, 6925-6932.
43. Samson, J. A. R.; Stolte, W. C., Precision Measurements of the Total Photoionization Cross-Sections of He, Ne, Ar, Kr, and Xe. *J. Electron Spectrosc. Relat. Phenom.* **2002**, *123*, 265-276.
44. Klippenstein, S. J., From Theoretical Reaction Dynamics to Chemical Modeling of Combustion. *Proc. Comb. Inst.* **2017**, *36*, 77-111.
45. Fernandes, R. X.; Luther, K.; Marowsky, G.; Rissanen, M. P.; Timonen, R.; Troe, J. r., Experimental and Modeling Study of the Temperature and Pressure Dependence of the Reaction $C_2h_5 + O2 (+ M) \rightarrow C_2h_5o_2 (+ M)$. *J. Phys. Chem. A* **2015**, *119*, 7263-7269.
46. Gans, B.; Garcia, G. A.; Boyé-Péronne, S.; Loison, J.-C.; Douin, S.; Gaie-Levrel, F. o.; Gauyacq, D., Absolute Photoionization Cross Section of the Ethyl Radical in the Range 8–11.5 Ev: Synchrotron and Vacuum Ultraviolet Laser Measurements. *J. Phys. Chem. A* **2011**, *115*, 5387-5396.
47. Kaiser, E., Temperature and Pressure Dependence of the C_2h_4 Yield from the Reaction $C_2h_5 + O_2$. *J. Phys. Chem.* **1995**, *99*, 707-711.
48. Dilger, H.; Schwager, M.; Tregenna-Piggott, P. L.; Roduner, E.; Reid, I. D.; Arseneau, D. J.; Pan, J. J.; Senba, M.; Shelley, M.; Fleming, D. G., Addition Kinetics and Spin Exchange in the Gas Phase Reaction of the Ethyl Radical with Oxygen. *J. Phys. Chem.* **1996**, *100*, 6561-6571.
49. Hashemi, H.; Jacobsen, J. G.; Rasmussen, C. T.; Christensen, J. M.; Glarborg, P.; Gersen, S.; van Essen, M.; Levinsky, H. B.; Klippenstein, S. J., High-Pressure Oxidation of Ethane. *Combust. Flame* **2017**, *182*, 150-166.
50. Meloni, G.; Zou, P.; Klippenstein, S. J.; Ahmed, M.; Leone, S. R.; Taatjes, C. A.; Osborn, D. L., Energy-Resolved Photoionization of Alkylperoxy Radicals and the Stability of Their Cations. *J. Am. Chem. Soc.* **2006**, *128*, 13559-13567.
51. Cool, T. A.; Wang, J.; Nakajima, K.; Taatjes, C. A.; Mcllroy, A., Photoionization Cross Sections for Reaction Intermediates in Hydrocarbon Combustion. *Int. J. Mass Spectrom.* **2005**, *247*, 18-27.